ELSEVIER

Nuclear Physics A616 (1997) 189c–200c

NUCLEAR PHYSICS A

# Elastic and inelastic scattering of exotic nuclei

A.A. Korsheninnikov[1*], E.A. Kuzmin[2], E.Yu. Nikolskii[2], C.A. Bertulani[3], O.V. Bochkarev[2], S. Fukuda[1], T. Kobayashi[1], S. Momota[1], B.G. Novatskii[2], A.A. Ogloblin[2], A. Ozawa[1], V. Pribora[2], I. Tanihata[1] and K. Yoshida[1]

[1] RIKEN, 2-1 Hirosawa, Wako, Saitama 351-01, Japan

[2] The Kurchatov Institute, Kurchatov sq. 1, Moscow 123182, Russia

[3] Universidade Federal do Rio de Janeiro, 21945-970 Rio de Janeiro, Brazil

[*] On leave from the Kurchatov Institute, Moscow 123182, Russia

Experimental studies of $^{11}$Li+p, $^{8}$He+p, $^{6}$He+p, $^{3}$H+p, and $^{14}$Be+p at $E \sim 65$ - 75 $A$ MeV are reported. The elastic scattering cross sections are measured. Effects of extended neutron distributions in $^{11}$Li, $^{8}$He, $^{6}$He are investigated. Spectroscopy of $^{11}$Li, $^{6}$He, $^{14}$Be is performed.

## 1. INTRODUCTION

We report on three recent experimental studies of the scattering of exotic nuclei by protons. In all the measurements we used binary radioactive beams produced by the fragment separator RIPS (RIKEN, Japan) and studied proton scattering for two neutron rich nuclei simultaneously. Namely, the following binary beams were used: $^{11}$Li and $^{8}$He, $^{6}$He and $^{3}$H, $^{11}$Li and $^{14}$Be.

## 2. SPECTROSCOPY OF $^{11}$Li. SCATTERING $^{11}$Li+p AND $^{8}$He+p

Numerous studies have been performed to investigate the structure of the ground state of the halo nucleus $^{11}$Li (e. g., see [1,2]). At the same time, questions about the $^{11}$Li ground state structure are related to possible excited states of $^{11}$Li. Corresponding experimental studies are especially important because a new type of excitation, the soft dipole mode, is expected to be a consequence of the neutron halo. However, reflecting experimental difficulties, the number of spectroscopic studies of $^{11}$Li is restricted to two only [3,4].

In Ref. [3], excited states of $^{11}$Li were searched for in the reaction $^{11}$B($\pi^-$,$\pi^+$)$^{11}$Li, and a weak manifestation of the $^{11}$Li excited state at $E^* = 1.2 \pm 0.1$ MeV was obtained, which was considered to be a candidate for the soft dipole excitation. In the second work [4], spectroscopy of $^{11}$Li was performed using the reactions $^{10}$Be($^{14}$C,$^{13}$N)$^{11}$Li and $^{14}$C($^{14}$C,$^{17}$F)$^{11}$Li. The observation of three excited states of $^{11}$Li was reported: at $E^* = 2.47 \pm 0.07$, $4.85 \pm 0.07$ and


PII: S0375-9474(97)00088-2

6.22 ± 0.07 MeV. These states were not seen in Ref. [3], while the $^{11}$Li state at $E^*$ ~ 1.2 MeV, which was reported in Ref. [3], was not observed in Ref. [4]. These circumstances as well as low statistics in the experimental data from Ref. [3] and high backgrounds from constituents of complex targets in the distributions from Ref. [4] prompted us to perform new spectroscopic study of $^{11}$Li by means of scattering $^{11}$Li+p [5]. The key point of the experiment was correlational measurement of emitted particles.

### 2.1. Experimental method

The secondary beam was produced by RIPS from fragmentation of the $^{18}$O primary beam at $E$ = 100 $A$ MeV on the $^{9}$Be target. The $^{11}$Li beam (intensity ~ 20 000 cps) had energy $E^{lab}$ = 74.5 $A$ MeV with broadening $\Delta$ = ± 3.0 $A$ MeV. The RIPS was tuned to produce a two component secondary beam. Apart from $^{11}$Li, it contained $^{8}$He at $E^{lab}$ = 66 $A$ MeV ($\Delta$ = ± 2 $A$ MeV), and we studied scattering $^{8}$He+p simultaneously with the spectroscopy of $^{11}$Li.

In these measurements under inverse kinematical conditions, we applied the missing mass method based on the detection of recoil proton both in an inclusive way and in coincidence with charged particles and neutrons from breakup of the projectile. The experimental setup is shown in Fig. 1. Two plastic scintillators were used for secondary-beam-particle identification and measurement of the beam energy. The trajectory of every beam particle was measured by two MWPCs. The secondary beam hit targets of $CH_2$ or C with thickness of 11.75 mg/cm$^2$ and 9.5 mg/cm$^2$, respectively. Note that all experimental distributions presented below correspond to the pure proton target (negligible background from the C target was subtracted).

To detect protons, we used two telescopes of solid state detectors with large area. Every telescope consisted of two strip detectors and three silicon detectors. The centers of the telescopes were located at 69°, i. e. in the range of small center-of-mass angles in the $^{11}$Li+p scattering. The telescopes measured the energy and angles of every proton, which allowed the determination of the energy in the residual $^{11}$Li-like system. The resolution in excitation energy of $^{11}$Li, FWHM ~ 1.5 MeV, was mainly determined by the angular resolution of the setup and the target thickness.

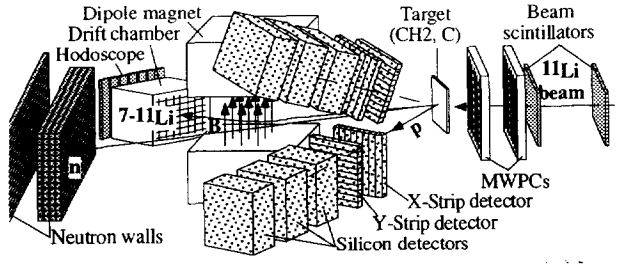


Fig. 1. The experimental setup.

Apart from recoil protons, we detected particles from the breakup of $^{11}$Li. Charged particles ($^{11}$Li, $^{9-7}$Li) were bent in the dipole magnet and measured by the drift chamber and the plastic scintillation counter hodoscope. Neutrons from decay of $^{11}$Li were detected by plastic scintillators. This part of the detection system allowed us to study exclusive spectra of protons in coincidence with Li-isotopes and neutrons.

### 2.2 Spectroscopy of $^{11}$Li

To obtain the resulting spectra presented in Fig. 2, we converted the measured distributions $d^2N/dE_p^{lab}d\Omega_p^{lab}$ into $d^2N/dE^*_{^{11}Li}d\Omega_p^{lab}$ and integrated them over the angles within the overall acceptance of the proton telescopes ($\theta_p^{lab}$ ~ 60°-80°).

The inclusive spectrum of protons from the process p($^{11}$Li,p) is presented in Fig. 2a. A strong peak corresponding to the $^{11}$Li ground state is seen. Typical physical backgrounds are illustrated by curves[1] which are smooth and follow the general trend in the high energy part of spectrum. Arrows in the Fig. 2a show positions of the $^{11}$Li excited states reported in Refs. [3,4]. Corresponding to arrows at higher energy, two peculiarities are seen in the experimental data, which are demonstrated in Fig. 2b in larger scale. The two arrows at lower energies in Fig. 2a are located in the region of the tail from the $^{11}$Li ground state, showing the necessity to investigate proton spectra detected in coincidence with particles from decay of $^{11}$Li. However, an interesting result can be already seen in the inclusive spectrum if we decrease bin size and improve the resolution by rejecting events with low energy protons (the resolution depends on the proton energy, in particular, because of the target thickness). The resultant spectrum presented in Fig. 2c shows a peculiarity in agreement with Ref. [3].

This peak is clearly seen with obvious statistical significance in Fig. 2d, where the solid histogram presents the proton spectrum detected in coincidence with $^{9}$Li (dotted histogram shows the elastic-scattering proton spectrum measured in coincidence p+$^{11}$Li). The same $^{11}$Li-peak at $E^* = 1.25 \pm 0.15$ MeV is observed in Fig. 2e and 2f also, where we show proton spectra from the processes p($^{11}$Li,p$^{9,8,7}$Li) and p($^{11}$Li,pn$^{9,8,7}$Li), respectively.

In Fig. 2d and 2e, a group on the right side from the 1.25-MeV peak attracts attention, which is located at the energy, $E^* = 3.0 \pm 0.2$ MeV. One more tentative

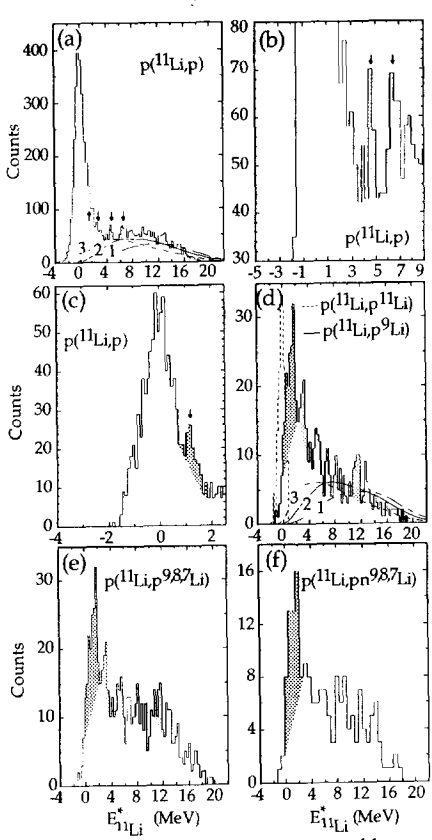


Fig. 2. Spectra of protons from scattering $^{11}$Li+p.

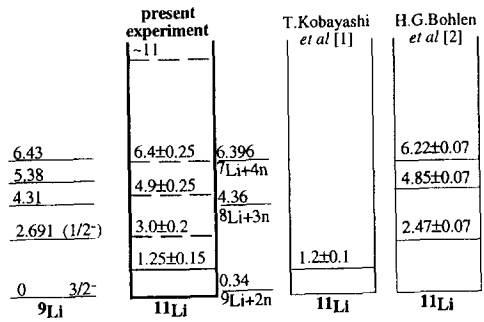


Fig. 3. Levels of $^{11}$Li.

[1] Curve 1 shows a phase space p+n+n+$^{9}$Li. Curve 2 presents final state interaction (virtual state) n+n or n+$^{9}$Li (corresponding to the low energy peak in $^{10}$Li [6,7]). Curve 3 shows an extreme case of low energy state of $^{10}$Li with negligible width. Detection acceptances and resolutions were included in the calculations.

group might be distinguished in Fig. 2d at $E^* = 4.9 \pm 0.25$ MeV confirming the left peak in Fig. 2b. Lastly, note a structure at $E^* \sim 11$ MeV in Fig. 2d. The corresponding peak can be seen in Ref. [4].

Finally, the peak at 1.25 MeV is statistically convincing. The smaller hatched peaks in Fig. 2 are less convincing, but together with the results of Ref. [4] the assignments of the corresponding states of $^{11}$Li seem plausible. All results are summarized in Fig. 3. Comparison with the levels of $^{9}$Li suggests that the 1.25-MeV-peak corresponds to the halo excitation.

### 2.3. Elastic scattering angular distributions

The measured angular distribution for the $^{11}$Li+p elastic scattering ($E^{lab} = 75\ A$ MeV) is shown in Fig. 4a, where the data obtained at 62 $A$ MeV [8] are presented also. Curves in Fig. 4a correspond to the optical model calculations for these two energies.

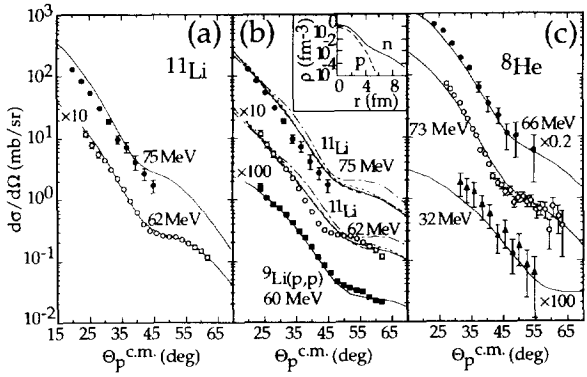


Fig. 4. Cross sections for elastic scattering p+$^{11}$Li, p+$^{9}$Li, p+$^{8}$He.

Elastic scattering data are often expected to provide new information about the halo structure. Below we study this problem considering four extreme assumptions about the valence neutrons' configurations in $^{11}$Li and analyze the experimental data using the eikonal approach[2] which contains no fitting parameters, unlike the optical model.

First, we calculated the angular distribution for the $^{9}$Li+p scattering at 60 $A$ MeV [8], which is shown in Fig. 4b. The curve presents a calculation with Gaussian proton and neutron densities with the same radii set equal to the experimental radius of $^{9}$Li. We also tried the shell-

---

2) We used the following amplitude for an elastic proton-nucleus scattering [11]:

$$f = ik\int J_0(e^{i\chi_C} - e^{i\chi_C+i\chi_N})bdb + f_C, \quad (1)$$

where $f_C(\theta)$ and $\chi_C$ are standard Coulomb amplitude and phase taken for a uniform charged sphere with $R_C = r_{0C}A^{1/3}$. The nuclear phase $\chi_N$ is determined by optical potential $V_N$ in the $t\rho$ approximation [11]:

$$\chi_N(b) = -\frac{1}{\hbar v}\int dz V_N(\sqrt{b^2+z^2}), \quad (2)$$

$$V_N = \bar{t}_{pn}\rho_n + \bar{t}_{pp}\rho_p,\ \bar{t}_{pN} = -\frac{\hbar v}{2}\bar{\sigma}_{pN}(\alpha_{pN}+i). \quad (3)$$

In Eq. (3), $\rho_{p(n)}$ is proton (neutron) density of nucleus. The Pauli-corrected pN total cross section, $\bar{\sigma}_{pN} = \sigma_{pN}P(\varepsilon_{NF}/\varepsilon)$, depends on the Fermi energy of target nucleon, $\varepsilon_{NF}$, calculated for $\rho_{p(n)}$. The energy $\varepsilon$ of incident proton at the interaction point was evaluated using the Coulomb potential and the real part of $V_N$.

In addition to $\rho_{p(n)}$, the input for the calculations includes parameters of the pN amplitude, $\sigma_{pN}$ and $\alpha_{pN}$. The pp and pn total cross sections, $\sigma_{pN}$, are known in the energy range under consideration, $E \le 100$ MeV; we fitted them by $\sigma_{pp}[mb] = 1/(-1.4\cdot10^{-3} + 4.45\cdot10^{-4}E - 7.37\cdot10^{-7}E^2)$ and $\sigma_{pn}[mb] = 1/(-2.5\cdot10^{-4} + 1.15\cdot10^{-4}E + 1.73\cdot10^{-7}E^2)$ ($E$ in MeV). Unlike $\sigma_{pN}$, parameters $\alpha_{pN}$ are known at $E \ge 100$ MeV [12]. We used simple interpolations, $\alpha_{pp} = 2.55 - 6.8\cdot10^{-3}E$ and $\alpha_{pn} = 1.08 - 8.0\cdot10^{-4}E$, from the values of $\alpha_{pN}$ [12] at two lowest energies.

model densities [13] with non-identical shapes for protons and neutrons; the result is close to the curve in Fig. 4b. As it is seen in the figure, the calculation produces a reasonable description of the experimental data. We shall use this approach to compare results obtained in different assumptions on the $^{11}$Li halo structure.

We used results from Ref. [14], where the $^{9}$Li+n+n model was applied in the cluster-orbital shell-model approximation (COSMA). The valence neutron density was taken for four extreme cases, two valence neutrons are in 1p, 2s, 1d, and 1s state[3]. Calculated cross sections for the $^{11}$Li+p scattering at 75 *A* and 62 *A* MeV are presented in Fig. 4b by solid, dotted, dashed, and dash-dotted curves corresponding to the valence neutrons in the 1p, 1s, 1d, and 2s state, respectively. The results are in satisfactory agreement with the experimental data. The curves for 1 $\ell$-states are very close to each other. The dash-dotted curve (2s) deviates from other results, but a difference of such a scale would be meaningful only after the appearance of high precision microscopic theory for elastic scattering. The curves in Fig. 4b correspond to the extreme cases with pure states. The performed calculations for more realistic mixtures between these configurations (these mixtures were discussed in Ref. [14]) gave results indistinguishable from the group of 1 $\ell$-curves in Fig. 4b. Thus, the investigation of sensitivity to the valence neutrons' configurations in $^{11}$Li has demonstrated that elastic scattering (at least at low energies) is not a very promising tool to study thin details of the halo structure.

In Fig. 4c, the measured angular distribution for the $^{8}$He+p elastic scattering at 66 *A* MeV is shown by black circles. Two other angular distributions in Fig. 4c at 73 *A* and 32 *A* MeV were measured previously [9,10]. Curves in the Fig. 4c show the above described eikonal calculations with the COSMA densities obtained in the $\alpha$+4n model for $^{8}$He [15]. The calculated cross sections are in a reasonable agreement with the experimental points. Note that detailed theoretical studies of the $^{8}$He+p scattering were performed in [16,17].

## 3. SCATTERING $^{6}$He+p AND $^{3}$H+p. EFFECTS OF NEUTRON SKIN AND HALO IN $^{6}$He, $^{8}$He, AND $^{11}$Li

Extended neutron distributions discovered in exotic neutron rich nuclei like, e. g., $^{11}$Li, $^{8}$He, $^{6}$He [1] sometimes are classified into two groups: skins and halos, reflecting the expectation of their different properties due to peculiar shapes of density profiles [1,18]. Here we report on measurements of proton elastic scattering by $^{6}$He as well as by the radioactive nucleus $^{3}$H (another study of the scattering $^{6}$He+p as well as $^{8}$He+p was recently carried out in [19]; data analysis is in progress). We perform a comparative analysis of all existing data on the proton scattering by $^{6}$He, $^{8}$He, $^{11}$Li. It turns out that the proton feels the valence neutrons in

---

3) These densities are determined by the following formulas:

$$\rho^{1p} = 2 \cdot 3^{-1} \pi^{-1.5} \alpha^{-3} x^2 e^{-x^2}, \quad (4)$$

$$\rho^{2s} = 2 \cdot 3^{-1} \pi^{-1.5} \alpha^{-3} (x^2 - 1.5)^2 e^{-x^2}, \quad (5)$$

$$\rho^{1d} = 4 \cdot 15^{-1} \pi^{-1.5} \alpha^{-3} x^4 e^{-x^2}, \quad (6)$$

$$\rho^{1s} = \pi^{-1.5} \alpha^{-3} e^{-x^2} \quad (7)$$

(in Ref. [14] it is argued that the 1s state for the halo neutrons is not straightforwardly forbidden in COSMA). In Eqs. (4-7), $x = r/\alpha$ and $\alpha$ corresponds to the radius of $^{11}$Li [14]. For the $^{9}$Li-core we used the Gaussian proton and neutron densities ( $R^{p}_{rms} = R^{n}_{rms} = R^{exp}_{mat}(^{9}Li)$ ).

$^{6}$He, $^{8}$He and does not feel them in $^{11}$Li, reflecting different properties of the skin ($^{6}$He, $^{8}$He) and the halo ($^{11}$Li).

### 3.1. Experimental results

We used radioactive beams of $^{6}$He and $^{3}$H and studied collisions $^{6}$He+p and $^{3}$H+p. The RIPS was tuned to produce the two component secondary beam, $^{6}$He and $^{3}$H, from fragmentation of $^{18}$O (100 *A* MeV) on the $^{9}$Be target. The $^{6}$He beam had energy $E^{lab}$ = 71 *A* MeV with energy spread $\Delta = \pm 3.0$ *A* MeV. The energy of the $^{3}$H beam was $E^{lab}$ =73.5 *A* MeV ($\Delta = \pm 4.5$ *A* MeV). The experimental method was the same as used for the above described studies of the scattering $^{11}$Li+p and $^{8}$He+p (see Fig. 1 for the setup).

The resulting proton spectra are presented in Fig. 5. The inclusive spectrum, p($^{6}$He,p), in Fig. 5A shows a strong peak from the $^{6}$He ground state. The arrow corresponds to the known excited state $^{6}$He$^{*}_{1.8}$ which is clearly seen in Fig. 5B in the spectrum of protons detected in coincidence with $^{4}$He. Figure 5C shows the inclusive spectrum, p($^{3}$H,p), where the elastic scattering peak is clearly seen. Note, that recently the excited state in $^{3}$H was suggested in the experimental study [20] (see also theoretical analysis [21]). Unfortunately, the spectrum in Fig. 5C does not allow the verification of this very interesting result.

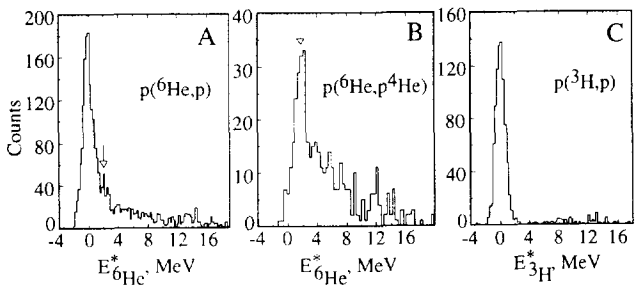


Fig. 5. Spectra of protons from scattering $^{6}$He+p and $^{3}$H+p.

The obtained angular distribution for elastic scattering $^{6}$He+p is presented in the middle of Fig. 6A, where we also show data for $^{8}$He+p (paragraph 2.3) and $^{4}$He+p [22] at the center-of-mass energies close to that for $^{6}$He+p. The results for $^{6}$He and $^{8}$He are similar to each other and differ essentially from that for $^{4}$He. Ratios to the Rutherford cross section show that the measured points correspond to the nuclear scattering. In such a situation, the slopes of the distributions usually reflect matter radii. Thus, the observed features of the experimental data show that

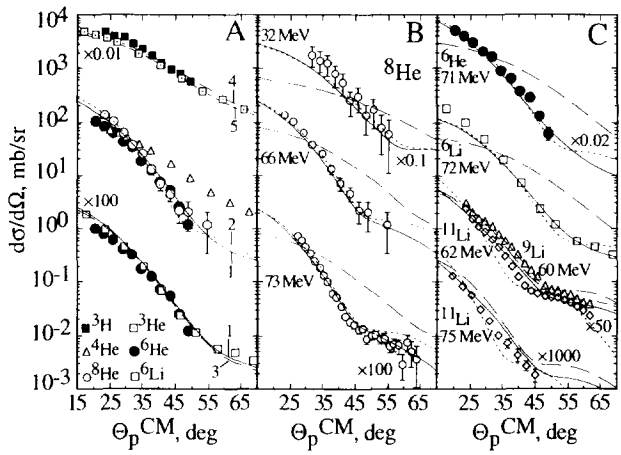


Fig. 6. Cross sections for elastic scattering $^{3}$H+p, $^{3}$He+p, $^{4}$He+p, $^{6}$He+p, $^{6}$Li+p, $^{8}$He+p, $^{9}$Li+p, $^{11}$Li+p (present experiments and [5,8-10,22-24]).

$^{6}$He and $^{8}$He have close radii greater than that of $^{4}$He in agreement with the known radii of these nuclei.

On the bottom of Fig. 6A we compare the $^{6}$He+p data with that for elastic scattering p+$^{6}$Li measured in [23] at almost the same energy of 72 MeV. These data are nearly identical, revealing a close similarity between gross characteristics of density distributions in $^{6}$He and $^{6}$Li. Note that the radii of $^{6}$He and $^{6}$Li are really close to each other, while a close analogy between the geometrical structures of $^{6}$He and $^{6}$Li is seen in three-body calculations.

The measured cross section for $^{3}$H+p is compared with data for p+$^{3}$He [24] on the top of Fig. 6A. Again, the results for $^{3}$H+p and $^{3}$He+p are in close agreement one with another in consistency with a belonging of $^{3}$H and $^{3}$He to the same isospin doublet.

### 3.2. Skin and halo

The performed measurement of elastic scattering $^{6}$He+p has enlarged the bank of experimental data on proton scattering by nuclei with neutron skins or halos. Figure 6B and 6C show all existing data for the proton elastic scattering by $^{8}$He, $^{6}$He and $^{11}$Li at different energies. In Fig. 6C we show also data for elastic scattering p+$^{6}$Li [23], which were included in our analysis because $^{6}$Li can be considered as having an α-core and an extended n+p distribution. We analyzed the data presented in Fig. 6 in the eikonal approach, which has no fitting parameters and provides connection with densities of nuclei. The method of calculations was the same as used in paragraph 2.3 for scattering $^{11}$Li+p and $^{8}$He+p. To investigate a sensitivity of elastic scattering to the neutron skin or halo, we considered for every nucleus $^{6}$He,$^{8}$He,$^{6}$Li, or $^{11}$Li three kinds of densities.

(I) The "*realistic*" densities correspond to the experimental matter radius of $^{6}$He,$^{8}$He,$^{6}$Li, or $^{11}$Li and contain the extended distribution of valence nucleons. These densities[4)] were derived in the cluster-orbital shell-model approximation (COSMA) [14].

(II) The "*non-halo*" densities neglect a difference between proton and neutron radii, but correspond to the experimental radius of $^{8}$He,$^{6}$He,$^{6}$Li, or $^{11}$Li. We used the Gaussian proton and neutron densities with identical radii equal to $R_{mat}$ of $^{6}$He, $^{8}$He, $^{6}$Li, or $^{11}$Li.

(III) The "*core-like*" densities. In this case we neglected the skin or halo and replaced the real radius of the nucleus by the radius of the core ($^{4}$He or $^{9}$Li). Namely, we used the Gaussian proton and neutron densities with identical radii equal to $R_{mat}$ of $^{4}$He or $^{9}$Li.

Results of calculations with the "*realistic*" densities shown in Fig. 6B and 6C by solid curves are in a reasonable agreement with all experimental data. Calculations with the "*non-halo*" densities are shown by dotted curves in Fig. 6B and 6C. These curves for $^{8}$He, $^{6}$He, $^{6}$Li (but

---

[4)] The $^{11}$Li densities obtained in [14] in the $^{9}$Li+2n model can be written as:

$$\rho_i(r) = N_{ci}\frac{exp(-r^2/a^2)}{\pi^{3/2}a^3} + N_{vi}\frac{2exp(-r^2/b^2)}{3\pi^{3/2}b^5}[Ar^2 + B(r^2 - \tfrac{3}{2}b^2)^2], \quad i=n,p, \tag{8}$$

($N_{cp}$=3, $N_{cn}$=6, $N_{vp}$=0, $N_{vn}$=2, $a$=1.89 fm, $b$=3.68 fm, $A$=0.81, $B$=0.19) for mixture of 1p- and 2s-orbitals for the valence neutrons, which reproduces experimental data on momentum distributions of $^{9}$Li from fragmentation of $^{11}$Li [14]. As it was mentioned in paragraph 2.3, different orbitals give results close to the solid curves for $^{11}$Li in Fig. 3C, which show calculations using (8).

The $^{8}$He densities derived in [15] in the α+4n model are given by (8) with $N_{vn}$=4, $N_{vp}$=0, $N_{cp}$ =$N_{cn}$=2, $a$=1.38 fm, $b$=1.99 fm, $A$=1, $B$=0.

For $^{6}$He and $^{6}$Li we applied the α+2N model. The results are given by (8), where $A$=1, $B$=0, $N_{cp}$=$N_{cn}$=2; $N_{vn}$=$N_{vp}$=1 for $^{6}$Li and $N_{vn}$=2, $N_{vp}$=0 for $^{6}$He; $a$=1.55 fm corresponding to a Gaussian density for $^{4}$He ($R_{mat}$=1.48 fm) folded with a Gaussian for the α-core motion, which is characterized by $R_{rms}$=1.2 fm for both $^{6}$He and $^{6}$Li [25,14]. Parameter $b$ was chosen to reproduce the experimental radius of $^{6}$He or $^{6}$Li.

not for $^{11}$Li) are close to the solid curves. At the same time, the dashed curves for the "*core-like*" densities differ drastically from the experimental data, solid and dotted curves for $^{8}$He, $^{6}$He and $^{6}$Li. Thus, the proton scattering is sensitive to a matter extension in $^{8}$He, $^{6}$He, $^{6}$Li in comparison with α-particle and it is insensitive to a difference between proton and neutron radii in $^{8}$He and $^{6}$He. Such regularities are different for the scattering $^{11}$Li+p. As it is seen in Fig. 6C, the solid curves are more similar to the dashed curves than to the dotted ones, showing that the $^{11}$Li+p scattering is determined to a large extent by the proton scattering on the $^{9}$Li-core reflecting a low density in the halo.

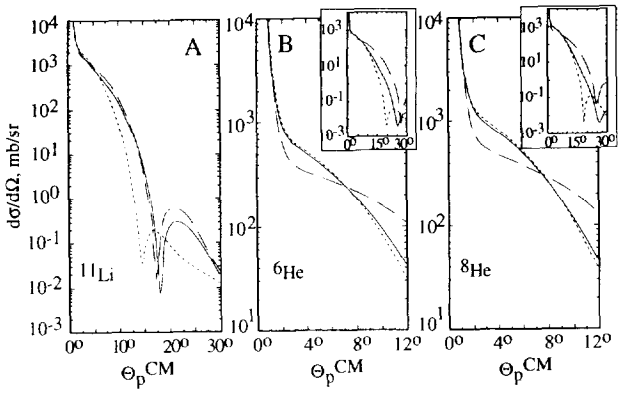


Fig. 7. Eikonal calculations for elastic scattering $^{11}$Li+p, $^{6}$He+p, and $^{8}$He+p at 800 *A* MeV.

The difference between $^{11}$Li and $^{6}$He, $^{8}$He is additionally confirmed in Fig. 6C by comparison of the $^{11}$Li data at 62 *A* MeV with the data for $^{9}$Li+p scattering [8] shown by triangles (the dashed-dotted curve shows the eikonal calculation for $^{9}$Li+p and describes the data well). These $^{11}$Li and $^{9}$Li distributions have very similar slopes and shapes (see also [26,27]) unlike the case of He-isotopes in the middle of Fig. 6A, where slope of the data for $^{4}$He differs essentially from that for $^{6,8}$He.

Such a distinction of $^{11}$Li from $^{8}$He, $^{6}$He remains at a high energy proton scattering. Figure 7A shows calculations for the $^{11}$Li+p scattering at 800 *A* MeV. The solid curve (the "*realistic*" density) is close in the wide angular range to the dashed curve (the "*core-like*" density) and both of them differ from the dotted curve (see also [28]). The situation is different for the proton scattering by $^{6}$He and $^{8}$He in Fig. 7B and 7C at angles $\leq 10^{o}$, where the solid curves are close to the dotted ones and differ from the dashed curves. At larger angles all three curves have distinctive behaviors (insets in Fig. 7B-7C) showing that the high energy proton scattering, being studied at relatively large angles, may allow the investigation of the $^{8}$He and $^{6}$He density profiles (see also [16]).

Thus, comparative analysis of the proton scattering by $^{6}$He, $^{6}$Li, $^{8}$He, $^{4}$He, $^{11}$Li, $^{9}$Li has revealed that (i) the scattering of $^{8}$He, $^{6}$He, $^{6}$Li feels the density extension in these nuclei in comparison with α-particle; (ii) on the contrary, the elastic scattering $^{11}$Li+p is mainly determined by the proton scattering on the $^{9}$Li-core being not sensitive to the neutron halo extended beyond the $^{9}$Li-core. These results form a basis for distinction between the neutron skin ($^{8}$He, $^{6}$He) and the neutron halo ($^{11}$Li). At the same time, as it was shown in paragraph 2.3, the proton elastic scattering seems not to be a very promising tool to study details of extended neutron distribution like, e. g., orbitals of valence neutrons in $^{11}$Li.

## 4. SCATTERING $^{11}$LI+p AND $^{14}$Be+p. EXCITATION WITH L=1 IN $^{11}$Li AND SPECTROSCOPY OF $^{14}$Be

We performed study of the $^{11}$Li+p scattering again. The experimental method was the same as used above (see Fig. 1 for the experimental setup). In this case, we had a full acceptance for the fragments $^{9}$Li (and $^{8}$Li, $^{7}$Li) emitted from breakup of $^{11}$Li and detected in coincidences with protons. Due to this we obtained angular distribution for the $^{11}$Li-peak at $E^*$ ~ 1.3 MeV.

Usage of binary secondary beam, $^{11}$Li and $^{14}$Be, has allowed us to perform a study of scattering $^{14}$Be+p simultaneously with investigation of $^{11}$Li. Since $^{14}$Be is known as a halo nucleus, such a study presents evident interest. Below we present preliminary results of these measurements.

### 4.1. Experimental results: energy spectra

The RIPS was tuned to produce the two component $^{11}$Li-$^{14}$Be-beam, but requirements for $^{14}$Be were predominant, because this beam is weaker. The $^{14}$Be beam had intensity of 3000 cps and energy $E^{lab}$ = 73.6 $A$ MeV with energy spread $\Delta$ = ±3.5 $A$ MeV. The $^{11}$Li beam had intensity of 12 000 cps and energy $E^{lab}$ = 68.4 $A$ MeV ($\Delta$ =±3.5 $A$ MeV). The targets of $CH_2$ and C had thicknesses of 48 mg/cm$^2$. They were thicker than in the above described experiments, because of weak beam of $^{14}$Be. Correspondingly, the resolution in excitation energy was FWHM ≈ 2 MeV.

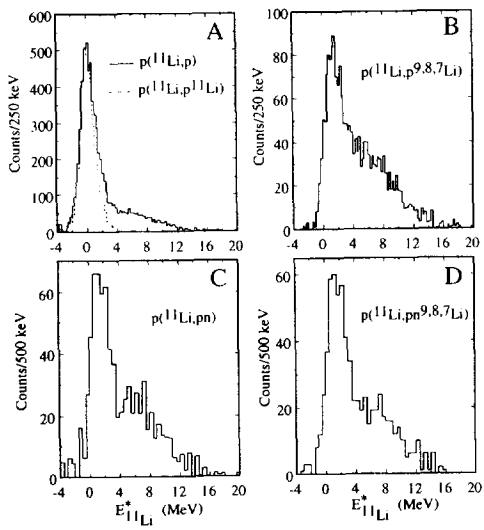


Fig. 8. Spectra of protons from scattering $^{11}$Li+p.

The spectra for the $^{11}$Li beam are presented in Fig. 8. In Fig. 8A, the solid histogram shows the inclusive spectrum of protons. A strong peak from the $^{11}$Li ground state is seen. The dotted histogram, which presents the spectrum of protons detected in coincidence p+$^{11}$Li, corresponds to the pure elastic scattering. It is seen that the left half of the dotted histogram coincides with the left side of the peak in the solid histogram, while on the right side the solid histogram exceeds the dotted one. It reflects the presence of the $^{11}$Li-peak at $E^*$ ~ 1.3 MeV. This peak is clearly seen in Fig. 8B - 8D for the nonelastic scattering events. Namely, Fig. 8B - 8D show proton spectra detected in coincidence p+$^{9,8,7}$Li, p+n, p+n+$^{9,8,7}$Li, respectively (among coincidences with Li-isotopes, the $^{9}$Li+p events are predominant). Parameters of the peak are in agreement with the measurements described in paragraph 2.2, $E^*$ = 1.3±0.1 MeV, $\Gamma$ = 0.75±0.6 MeV. Other (tentative) states mentioned if Fig. 3 might not be seen due to resolution and lower cross sections than that for the 1.3-MeV peak.

Proton spectra for the $^{14}$Be beam are presented in Fig. 9. In Fig. 9A, where the inclusive proton spectrum is shown, the elastic scattering peak is seen. Figures 9B - 9D correspond to

nonelastic events and show proton spectra detected in coincidence p+$^{12}$Be, p+n, and p+n+$^{12}$Be, respectively. In Fig. 9B - 9D, the $^{14}$Be excited state at $E^* = 1.6 \pm 0.1$ MeV is seen (it is in agreement with [29]) as well as a weaker peak at $E^* = 4.1 \pm 0.2$ MeV.

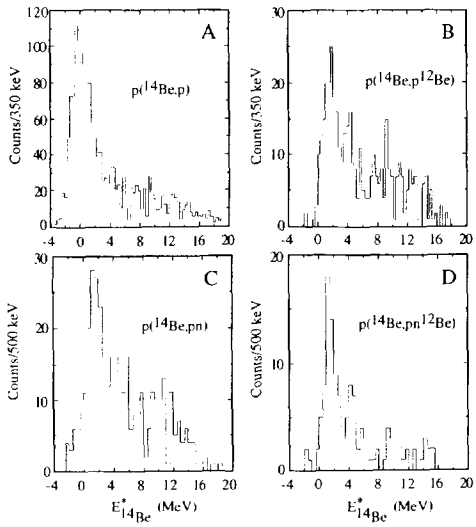


Fig. 9. Proton spectra from scattering $^{14}$Be+p.

## 4.2. Angular distributions for scattering $^{11}$Li+p

Angular distributions for the elastic scattering $^{11}$Li(p,p)$^{11}$Li and for excitation of the $^{11}$Li-peak at $E^* \sim 1.3$ MeV are presented in Fig. 10. Analysis of the data was performed using coupled-channel calculations. The results[5] are shown in Fig. 10 for transferred orbital angular momentum $L = 0, 1, 2, 3$. It is seen that the experimental data are consistent with $L = 1$. Note, that a hint of the $L = 1$ excitation was obtained in [3]. Lets us present simple considerations of corresponding configurations in $^{11}$Li.

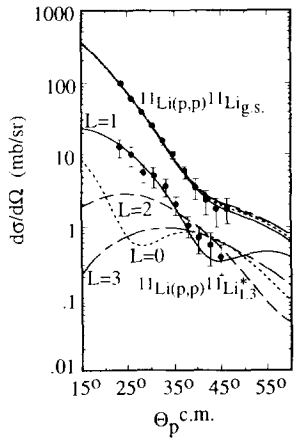


Fig. 10. Angular distributions for scattering $^{11}$Li+p.

Omitting the spin of the $^9$Li-core, the configuration with $L = 1$ in the system n+n+$^9$Li could reflect a predominance of the following component[6] of the wave function:

$$\left| l_{n-n} = S_{nn} = 0, l_{^9Li-nn} = 1, L = 1, J^\pi = 1^- \right\rangle. \qquad (9)$$

It contains a component with $\ell = 1$ in the n+$^9$Li subsystem. For example, in the K-harmonics' approach, for the minimal hypermomentum $K = 1$, the wave function (9) corresponds to a mixture of s- and p-states in n+$^9$Li with weights of 45% and 55%, respectively, determined by the Reinal-Revai coefficients. According to modern understanding, there are s- and p-resonances in $^{10}$Li. As a result, the state (9) could be stressed by the attraction between n+$^9$Li corresponding to the $^{10}$Li resonances as well as by the attraction between two

[5] In Fig. 10, the results are shown on an example of calculations using the code ECIS with optical potential parameters $V_r = 27.366$ MeV, $r_{or} = 1.025$ fm, $a_r = 0.727$ fm, $W_s = 19.944$ MeV, $r_{os} = 0.781$ fm, $a_s = 0.877$ fm, $W_d = 1.740$ MeV, $r_{od} = 0.960$ fm, $a_d = 1.222$ fm, $V_{so} = 7.370$ MeV, $r_{o\text{-}so} = 0.573$ MeV, $a_{so} = 0.412$ fm. In this case, in the fitting procedure, we used results of Ref. [26] for starting potential.

[6] Here $l_{a\text{-}b}$ is orbital momentum between particles $a$ and $b$, $l_{c\text{-}ab}$ is orbital momentum between particle $c$ and center of mass of $a$ and $b$, $S_{nn}$ is summary spin of two neutrons, $\hat{L} = \hat{l}_{a\text{-}b} + \hat{l}_{ab\text{-}c}$, $\hat{J} = \hat{L} + \hat{S}_{nn}$.

neutrons corresponding to the virtual singlet state. Other ways to get configuration with $L = 1$ at $K = 1$ correspond to the following three cases:

$$\left| l_{n-n} = S_{nn} = 1, l_{^9Li-nn} = 0, L = 1, J = \hat{1} + \hat{1} \right\rangle \qquad (10)$$

for $J^\pi = 0^-$, $1^-$ and $2^-$.The configurations (10) again can be stressed by the attraction between n+$^9$Li, because they also correspond to a mixture of s- and p-motion in n+$^9$Li (55% and 45%, respectively), but they are not supported by nn-forces ($l_{n-n} = 1$).

Since every wave function (9) - (10) contains component with p-state in n+$^9$Li, we need to study j-states in n+$^9$Li. Using 9J-symbols, and one can find that (9) and (10) at $J^\pi = 1^-$ and $2^-$ contain strong P3/2-component for n+$^9$Li. That is why we need to exclude them due to the Pauli principle (P3/2-orbital is occupied in $^9$Li). The only wave, which contains P1/2 for n+$^9$Li and does not contain P3/2 at $K$=1, is the wave (10) with $J^\pi = 0^-$.

However, to get a final conclusion, one more step is needed. Considering $K = 1$, we found that (9) and (10) contains n+$^9$Li in s-state. Since it should be 2s-state (1S1/2-orbital is occupied in $^9$Li), the minimal hypermomentum is $K = 3$. That is why we need to study waves (9) - (10) at $K = 3$ as well as four additional waves with orbital momenta in subsystems $l = 2$. Using the above illustrated technique to perform transitions to j-states in n+$^9$Li, we found that the P3/2 state in n+$^9$Li is excluded only in the mixture of the wave function (10) at $J^\pi = 0^-$ with the wave function $\left| l_{n-n} = S_{nn} = 1, l_{^9Li-nn} = 2, L = 1, J^\pi = 0^- \right\rangle$. This result provides again $J^\pi = 0^-$ and corresponds to a mixture of s- and p-motion in n+$^9$Li (42% and 57%, respectively; d-wave is weak, 1.7%). Finally, in the total wave function, higher order terms with larger K should be suppressed due to the increasing of the three-body centrifugal barrier [25].

Thus, the observed 1.3-MeV-peak is consistent with the $0^-$-configuration in the system n+n+$^9$Li. After taking into account spin $3/2^-$ of $^9$Li, the total $J^\pi$ becomes $3/2^+$. For further investigation of the configuration of 1.3-MeV-peak the dynamical three-body calculations are needed. However, a deficient information on the $^9$Li+p interaction can provide problems for such calculations.

## 5. SUMMARY

We have measured angular distributions for elastic scattering $^{11}$Li+p, $^8$He+p, $^6$He+p, $^3$H+p at 65 - 75 $A$ MeV. The measured cross sections as well as other existing data for elastic scattering $^{11}$Li+p, $^9$Li+p, $^8$He+p, $^6$Li+p were analyzed in the parameter-free eikonal approach, and a reasonable description of the experimental data was found.

Comparative analysis of the proton scattering by $^4$He, $^6$He, $^6$Li, $^8$He, $^9$Li, and $^{11}$Li has revealed that (i) the scattering of $^8$He, $^6$He, $^6$Li feels the density extension in these nuclei in comparison with $^4$He; (ii) on the contrary, the elastic scattering $^{11}$Li+p is mainly determined by the proton scattering on the $^9$Li-core being not sensitive to the neutron halo extended beyond the $^9$Li-core. These results form a basis for a distinction between the neutron skin ($^8$He, $^6$He) and the neutron halo ($^{11}$Li). At the same time, the investigation of the sensitivity to the valence neutrons' configurations in $^{11}$Li has demonstrated that elastic scattering at low energies is not very promising tool to study such details of halos.

The measured proton spectra show the well known excited state $^6$He$^*_{1.8}$, the $^{14}$Be excited state at $E^* = 1.6 \pm 0.1$ MeV and a weaker $^{14}$Be-peak at $E^* = 4.1 \pm 0.2$ MeV. For $^{11}$Li, the

proton spectra definitely show the peak at $E^* \sim 1.3$ MeV. In addition, four other states (Fig. 3) were assigned to $^{11}$Li tentatively; at the same time, some of these states are consistent with existing measurements [4]. Angular distribution measured for the 1.3-MeV-peak of $^{11}$Li show the $L = 1$ transition, and this peak is consistent with configuration $0^-$ in the system n+n+$^9$Li (omitting spin of $^9$Li) corresponding to a total $J^\pi = 3/2^+$ (taking into account spin-parity of $^9$Li).

## REFERENCES


1. I. Tanihata, Prog. Part. Nucl. Phys., **35** (1995) 505.
2. H. Geissel, G. Munzenberg, K. Riisager, Annu. Rev. Nucl. Part. Sci. **45** (1995) 163.
3. T. Kobayashi, Nucl. Phys. **A538** (1992) 343c.
4. H.G. Bohlen, R. Kalpakchieva, D.V. Aleksandrov *et al*, Z. Phys. **A351** (1995) 7.
5. A.A.Korsheninnikov, E.Yu.Nikolskii, T.Kobayashi *et al*, Phys.Rev. **C53** (1996) R537.
6. A.I. Amelin, M.G. Gornov, Yu.B. Gurov *et al*, Sov. J. Nucl. Phys. **52** (1990) 782.
7. R.A. Kryger, A. Azhari, A. Galonsky *et al*, Phys. Rev. **C47** (1993) R2439.
8. C.-B. Moon, M. Fujimaki, S. Hirenzaki *et al*, Phys. Lett. **B297** (1992) 39.
9. A.A. Korsheninnikov, K.Yoshida, D.V.Aleksandrov *et al*, Phys. Lett. **B316** (1993) 38.
10. A.A. Korsheninnikov, E.Yu.Nikolskii, T.Kobayashi *et al*, Phys. Lett. **B343** (1995) 53.
11. C.A. Bertulani, L.F. Canto, M.S. Hussein, Phys. Rep. **226** (1993) 281.
12. L. Ray, Phys. Rev. **C20** (1979) 1857.
13. G.F. Bertsch, B.A. Brown, H. Sagawa, Phys. Rev. **C39** (1989) 1154.
14. M.V. Zhukov, B.V. Danilin, D.V. Fedorov *et al*, Phys. Rep. **231** (1993) 151.
15. M.V. Zhukov, A.A. Korsheninnikov, M.H. Smedberg, Phys. Rev. **C50** (1994) R1.
16. L.V. Chulkov, C.A. Bertulani, A.A. Korsheninnikov, Nucl. Phys. **A587** (1995) 291.
17. R. Crespo, J.A. Tostevin, R.C. Johnson, Phys. Rev. **C51** (1995) 3283.
18. K. Riisager, Rev. Mod. Phys. **66** (1994) 1105.
19. S. Neumaier, G.D. Alkhazov, M.N. Andronenko *et al.*, Nucl. Phys. **A583** (1995) 799c.
20. D. Aleksandrov, E. Nikolskii, B. Novatskii, D. Stepanov, JETP Lett. **59** (1994) 320.
21. A.L. Barabanov, JETP Lett., **61** (1995) 7.
22. S. Burzynski, J. Campbell, M. Hammans *et al.*, Phys. Rev. **C39** (1989) 56.
23. R. Henneck, G. Masson, P.D. Eversheim *et al.*, Nucl. Phys. **A571** (1994) 541.
24. L.G. Votta, P.G. Roos, N.S. Chant, R. Woody, III, Phys. Rev. **C10** (1974) 520.
25. B.Danilin, M.Zhukov, A.Korsheninnikov, L.Chulkov, Sov.J.Nucl.Phys. **53** (1991) 45.
26. S. Hirenzaki, H. Toki, I. Tanihata, Nucl. Phys. **A552** (1993) 57.
27. Y. Suzuki, K. Yabana, Y. Ogawa, Phys. Rew. **C47** (1993) 1317.
28. G.D.Alkhazov, A.A.Lobodenko, Phys. At. Nuclei 56 (1993) 337.
29. W. von Oertzen, H.G. Bohlen, B. Gebauer *et al.*, Nucl. Phys. **A588** (1995) 129c.